

## RESEARCH ARTICLE

## ATOMIC PHYSICS

# The Rydberg constant and proton size from atomic hydrogen

Axel Beyer,<sup>1</sup> Lothar Maisenbacher,<sup>1\*</sup> Arthur Matveev,<sup>1</sup> Randolph Pohl,<sup>1†</sup> Ksenia Khabarova,<sup>2,3</sup> Alexey Grinin,<sup>1</sup> Tobias Lamour,<sup>1</sup> Dylan C. Yost,<sup>1‡</sup> Theodor W. Hänsch,<sup>1,4</sup> Nikolai Kolachevsky,<sup>2,3</sup> Thomas Udem<sup>1,4</sup>

At the core of the “proton radius puzzle” is a four-standard deviation discrepancy between the proton root-mean-square charge radii ( $r_p$ ) determined from the regular hydrogen (H) and the muonic hydrogen ( $\mu p$ ) atoms. Using a cryogenic beam of H atoms, we measured the 2S-4P transition frequency in H, yielding the values of the Rydberg constant  $R_\infty = 10973731.568076(96)$  per meter and  $r_p = 0.8335(95)$  femtometer. Our  $r_p$  value is 3.3 combined standard deviations smaller than the previous H world data, but in good agreement with the  $\mu p$  value. We motivate an asymmetric fit function, which eliminates line shifts from quantum interference of neighboring atomic resonances.

The study of the hydrogen atom (H) has been at the heart of the development of modern physics. Precision laser spectroscopy of H is used today to determine fundamental physical constants such as the Rydberg constant  $R_\infty$  and the proton charge radius  $r_p$ , defined as the root mean square (RMS) of its charge distribution. Owing to the simplicity of H, theoretical calculations can be carried out with astonishing accuracy, reaching precision up to the 12th decimal place. At the same time, high-resolution laser spectroscopy experiments deliver measurements with even higher accuracy, reaching up to the 15th decimal place in the case of the 1S-2S transition (*1, 2*), the most precisely determined transition frequency in H.

The energy levels in H can be expressed as

$$E_{nlj} = R_\infty \left( -\frac{1}{n^2} + f_{nlj} \left( \alpha, \frac{m_e}{m_p}, \dots \right) + \delta_{l0} \frac{C_{NS}}{n^3} r_p^2 \right) \quad (1)$$

where  $n$ ,  $l$ , and  $j$  are the principal, orbital, and total angular momentum quantum numbers, respectively. The first term describes the gross structure of H as a function of  $n$  and was first observed in the visible H spectrum and explained empirically by Rydberg. Later, the Bohr model, in which the electron is orbiting a pointlike and, in simplest approximation, infinitely heavy proton, provided a deeper theoretical understanding.

The Rydberg constant  $R_\infty = m_e \alpha^2 c / 2h$  links the natural energy scale of atomic systems and the SI unit system. It connects the mass of the electron  $m_e$ , the fine structure constant  $\alpha$ , Planck's constant  $h$ , and the speed of light in vacuum  $c$ . Precision spectroscopy of H has been used to determine  $R_\infty$  by means of Eq. 1 with a relative uncertainty of 6 parts in  $10^{12}$ , making it one of the most precisely determined constants of nature to date and a cornerstone in the global adjustment of fundamental constants (*3*).

The second term in Eq. 1,  $f_{nlj}(\alpha, \frac{m_e}{m_p}, \dots) = X_{20}\alpha^2 + X_{30}\alpha^3 + X_{31}\alpha^3 \ln(\alpha) + X_{40}\alpha^4 + \dots$ , accounts for relativistic corrections, contributions coming from the interactions of the bound-state system with the quantum electrodynamics (QED) vacuum fields, and other corrections calculated in the framework of QED (*3*). The electron-to-proton mass ratio  $m_e/m_p$  enters the coefficients  $X_{20}$ ,  $X_{30}$ , ... through recoil corrections caused by the finite proton mass.

The last term in Eq. 1 with coefficient  $C_{NS}$  is the leading-order correction originating from the finite charge radius of the proton,  $r_p$  (*3*). It only affects atomic S states (with  $l = 0$ ) for which the electron's wave function is nonzero at the origin. Higher-order nuclear charge distribution contributions are included in  $f_{nlj}(\alpha, \frac{m_e}{m_p}, \dots)$ .

## The proton radius puzzle

The proton charge radius  $r_p$  has been under debate for some time now because the very accurate value from laser spectroscopy of the exotic muonic hydrogen atom ( $\mu p$ ) (*4, 5*) yielded a value that is 4%, corresponding to  $5.6\sigma$ , smaller than the CODATA 2014 value of  $r_p$  (*3*) [see (*6–8*) for reviews on this issue]. The CODATA value is obtained from a combination of 24 transition frequency measurements in H and deuterium and several results from elastic electron scattering (*9–11*). The accuracy of the  $\mu p$  result is enabled by the fact that the muon's orbit is  $\sim 200$  times

smaller than the electron's orbit in H, resulting in a seven orders of magnitude larger influence of  $r_p$  on the energy levels.

Here we study the spectroscopic part of the discrepancy, in particular the  $4\sigma$  discrepancy between the  $\mu p$  value and the global average of all transitions measured in H (*12*) (H world data, Fig. 1). Recently, a similar discrepancy has arisen for the deuteron radius with a new result from laser spectroscopy of muonic deuterium (*13*).

Considering Eq. 1 and the fact that  $f_{nlj}(\alpha, \frac{m_e}{m_p}, \dots)$  is known with sufficiently high accuracy, one finds a very strong correlation between  $R_\infty$  and  $r_p$ . CODATA quotes a correlation coefficient of 0.9891. Equation 1 involves two parameters,  $R_\infty$  and  $r_p$ , which need to be determined simultaneously from a combination of at least two measurements in H. The 1S-2S transition frequency serves as a cornerstone in this procedure. Owing to its small natural line width of only 1.3 Hz, experimental determinations are one thousand times more accurate than for any other transition frequency in H, where typical line widths amount to 1 MHz or more.

Examining previous determinations of the value pairs  $[R_\infty, r_p]$  from H (Fig. 1, bottom), one notes that many of the individual measurements are in fact not in disagreement with the  $\mu p$  value. The discrepancy of  $4\sigma$  appears when averaging all H values ( $\mu p$  versus H world data; Fig. 1, top).

## Principle of the measurement

Here we report on a measurement of the 2S-4P transition in H (Fig. 2A), yielding  $[R_\infty, r_p]$  with an uncertainty comparable to the aggregate H world data and significantly smaller than the proton radius discrepancy, which corresponds to 8.9 kHz in terms of the 2S-4P transition frequency. This uncertainty requires a determination of the resonance frequency to almost one part in 10,000 of the observed line width of 20 MHz (Fig. 2B).

The previous most accurate measurements [see, e.g., (*14–16*) and references therein] were limited by the electron-impact excitation used to produce atoms in the metastable 2S state. This excitation results in hot atoms with mean thermal velocities of 3000 m/s or more and an uncontrolled mixture of population in the four 2S Zeeman sublevels. In turn, this typically leads to corrections on the order of tens of kilohertz because of effects such as the second-order Doppler and ac-Stark shifts or the excitation of multiple unresolved hyperfine components.

Our measurement is essentially unaffected by these systematic effects (*17*) because we use the Garching 1S-2S apparatus (*1, 2*) (Fig. 3) as a well-controlled cryogenic source of 5.8-K cold 2S atoms. Here, Doppler-free two-photon excitation is used to almost exclusively populate the  $2S_{1/2}^{F=0}$  Zeeman sublevel without imparting additional momentum on the atoms.

The remaining main systematic effects in our experiment are the first-order Doppler shift and apparent line shifts caused by quantum interference of neighboring atomic resonances, both of

<sup>1</sup>Max-Planck-Institut für Quantenoptik, 85748 Garching, Germany. <sup>2</sup>P.N. Lebedev Physical Institute, 119991 Moscow, Russia. <sup>3</sup>Russian Quantum Center, 143025 Skolkovo, Russia. <sup>4</sup>Ludwig-Maximilians-Universität, 80539 München, Germany. \*Corresponding author. Email: lothar.maisenbacher@mpq.mpg.de <sup>†</sup>Present address: Johannes Gutenberg-Universität Mainz, 55122 Mainz, Germany. <sup>‡</sup>Present address: Colorado State University, Fort Collins, CO 80523, USA.

which are suppressed by using methods specifically developed for this measurement and detailed below.

### Quantum interference

Line shape distortions caused by quantum interference from distant neighboring atomic resonances have recently come into the focus of the precision spectroscopy community (18). To the best of our knowledge, this effect has been considered in the analysis of only one of the previous H experiments and was found to be unimportant for that particular experimental scheme (19). The effect was found to be responsible for discrepan-

cies in the value of the fine structure constant  $\alpha$  extracted from various precision spectroscopy experiments in helium (20, 21). The root of the matter is that natural line shapes of atomic resonances may experience deviations from a perfect Lorentzian when off-resonant transitions are present. One common way of dealing with these effects has been to perform sophisticated numerical simulations to correct the experimental results (18, 20, 22–26). These simulations require a highly accurate characterization of the experimental geometry if the line center needs to be determined with high accuracy relative to the line width, as is the case in this measure-

ment. Here we remove this necessity and a source of potential inaccuracies by a suitable line shape model to compensate for the line shape distortions.

### Two driven oscillators

Within the framework of perturbation theory, the induced dipole moment  $\vec{D}(\omega)$  of an atom driven by a laser field  $\vec{E}$  at frequency  $\omega$  is given by the Kramers-Heisenberg formula (27–29). For two resonances at  $\omega_0$  and  $\omega_0 + \Delta$  with identical damping constants  $\Gamma$ , the resulting dipole moment is given by

$$\vec{D}(\omega) \propto \frac{\vec{D}_0}{(\omega_0 - \omega) + i\Gamma/2} + \frac{\vec{D}_1}{(\omega_0 + \Delta - \omega) + i\Gamma/2} \quad (2)$$

It is analogous to two coherently driven resonating classical dipoles  $\vec{D}_0$  and  $\vec{D}_1$ . In the quantum description, each of these dipoles is constructed through an absorbing and an emitting dipole, connecting the initial state ( $|i\rangle$ ) with the final state ( $|f\rangle$ ) via the excited states ( $|e\rangle, |e'\rangle$ ) (see Fig. 2A). With the atomic dipole matrix elements  $d_{jk}$  with  $j, k \in i, e, e', f$ , the contributing dipole moments are given by  $\vec{D}_0 \propto (\vec{E} \cdot \vec{d}_{ie})\vec{d}_{ef}$  and  $\vec{D}_1 \propto (\vec{E} \cdot \vec{d}_{ie'})\vec{d}_{ef}$ . The induced dipole  $\vec{D}(\omega)$  generates a field  $\propto (\vec{r} \times \vec{D}(\omega)) \times \vec{r}/|\vec{r}|^3$  at position  $\vec{r}$  whose power spectrum  $P(\omega, \vec{r})$  is proportional to the square modulus of  $\vec{D}(\omega)$ . It consists of two real valued Lorentzians and a non-Lorentzian cross term. The latter depends not only on the relative orientation of  $\vec{D}_0$  and  $\vec{D}_1$  but also on the direction of the emitted radiation relative to the orientation of the dipoles. Because the orientation of the dipoles is itself a function of the laser polarization, i.e., the orientation of  $\vec{E}$ , the observed cross term will effectively depend on the orientation of the laser polarization relative to detection direction. If the detection is not pointlike, as is the case in our measurement, which is designed for an as-large-as-possible collection efficiency, the exact detection geometry will enter in the observed cross term. The relative strength of the cross term tends to decrease with increasing detection solid angle, with the cross term completely disappearing for detection of all radiation emitted, i.e., in a  $4\pi$  solid angle.

For a sufficiently large separation of the two resonances ( $\Gamma/\Delta \ll 1$ ), the second resonance at  $\omega_0 + \Delta$  can be treated as a perturbation to the resonance at  $\omega_0$  and the full line shape  $P(\omega, \vec{r})$  can be expanded around the resonance at  $\omega_0$  (28)

$$P(\omega, \vec{r}) \approx \frac{C}{(\omega - \omega_0)^2 + (\Gamma/2)^2} + a(\omega - \omega_0) + \frac{b(\omega - \omega_0)}{(\omega - \omega_0)^2 + (\Gamma/2)^2} \quad (3)$$

The first term represents the Lorentzian line shape with amplitude  $C$  of the isolated, unperturbed resonance at  $\omega_0$ , whereas the other two terms denote perturbations caused by the presence of the second resonance. The second term,

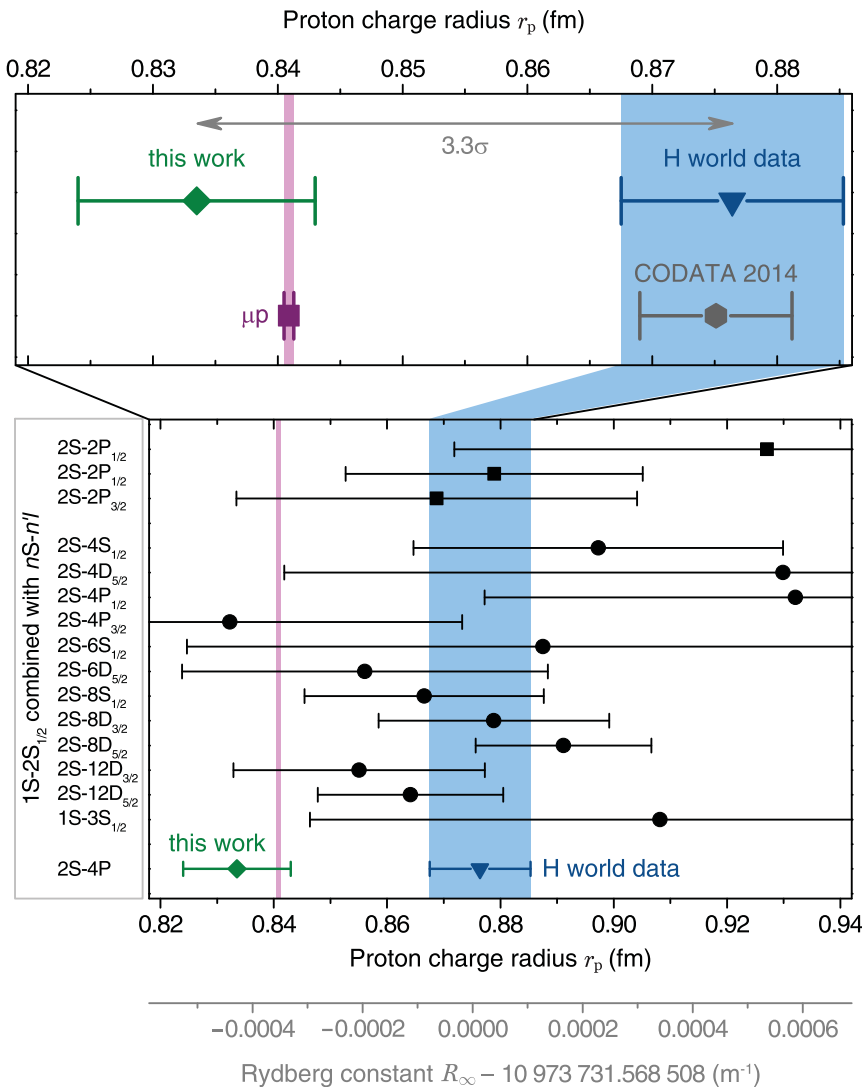


**Fig. 1. Rydberg constant  $R_\infty$  and proton RMS charge radius  $r_p$ .** Values of  $r_p$  derived from this work (green diamond) and spectroscopy of  $\mu p$  ( $\mu p$ ; pink bar and violet square) agree. We find a discrepancy of 3.3 and 3.7 combined standard deviations with respect to the H spectroscopy world data (12) (blue bar and blue triangle) and the CODATA 2014 global adjustment of fundamental constants (3) (gray hexagon), respectively. The H world data consist of 15 individual measurements (black circles, optical measurements; black squares, microwave measurements). In addition to H data, the CODATA adjustment includes deuterium data (nine measurements) and elastic electron scattering data. An almost identical plot arises when showing  $R_\infty$  instead of  $r_p$  because of the strong correlation of these two parameters. This is indicated by the  $R_\infty$  axis shown at the bottom.

linear in  $\omega$  and of amplitude  $a$ , accounts for the resonance of interest sitting on the far-reaching Lorentzian tail of the perturbing resonance. The dispersive-shaped third term stems from the non-Lorentzian cross term and accounts for the quantum interference between the resonances, with the dependence of the cross term on the detection geometry now absorbed in the amplitude  $b$ . For a typical fluorescence-detection geometry, the line shifts caused by the coherent third term may be much larger than the ones caused by the incoherent second term.

The emergence of asymmetric line shapes because of interference between a resonant and a nonresonant process is perhaps best known from Fano resonances (30), where a background and a resonant scattering process interfere. It should not then be surprising that Eq. 3 is very similar to the line shape of Fano resonances.

Neglecting the influence of the perturbing resonance and thus the quantum interference between the resonances, e.g., by a fit of the spectrum  $P(\omega, \vec{r})$  with a single Lorentzian, leads to apparent shifts of the determined line center of approximately (28)

$$\Delta\omega = \frac{b\Gamma^2}{4C} + \frac{a\Gamma^4}{8C} \approx -\frac{\vec{D}_0 \cdot \vec{D}_1}{2D_0^2} \frac{\Gamma^2}{\Delta} + \mathcal{O}\left(\frac{\Gamma^4}{\Delta^3}\right) \quad (4)$$

Typical values of  $\Gamma^2/\Delta$  are on the order of  $10^{-2} \Gamma$  for the transitions listed for H in Fig. 1. This is one order of magnitude larger than the proton radius discrepancy, which amounts to about  $10^{-3} \Gamma$  or less for all individual  $2S-nl$  measurements in Fig. 1. However, these measurements do not detect the emitted radiation (but rather the surviving 2S population), which diminishes the effect of quantum interference drastically at the cost of a reduced signal-to-noise ratio. The second term in Eq. 4, which stems from the term proportional to  $a$  in Eq. 3, is much smaller (on the order of  $10^{-6} \Gamma$ ) and may be safely ignored at this point. Importantly, the shift changes sign when exchanging  $\vec{D}_0$  and  $\vec{D}_1$  and replacing  $\Delta$  with  $-\Delta$ , i.e., the two resonances always shift in opposite directions. Thus, by combining measurements of both resonances with appropriate weights, the shift may be drastically reduced or even canceled, a fact we will make use of below.

### Atomic line shape model

For the 2S-4P transition in H, the role of the mutually perturbing resonances is played by the two dipole-allowed transitions to the fine structure components of the excited state, 2S-4P<sub>1/2</sub> and 2S-4P<sub>3/2</sub> (Fig. 2). Somewhat analogous to Young's double-slit experiment, the atom can coherently evolve from the initial 2S state, through any of the two 4P fine structure components, before finally reaching the 1S ground state. Given the separation between the two components,  $\Delta = 106 \times \Gamma$ , and the natural line width,  $\Gamma = 2\pi \times 12.9$  MHz, Eq. 4 predicts apparent, geometry-dependent line shifts of up to  $\sim 120$  kHz. With our large solid angle detectors, the maximum

**Fig. 2. Hydrogen 2S-4P spectroscopy.**

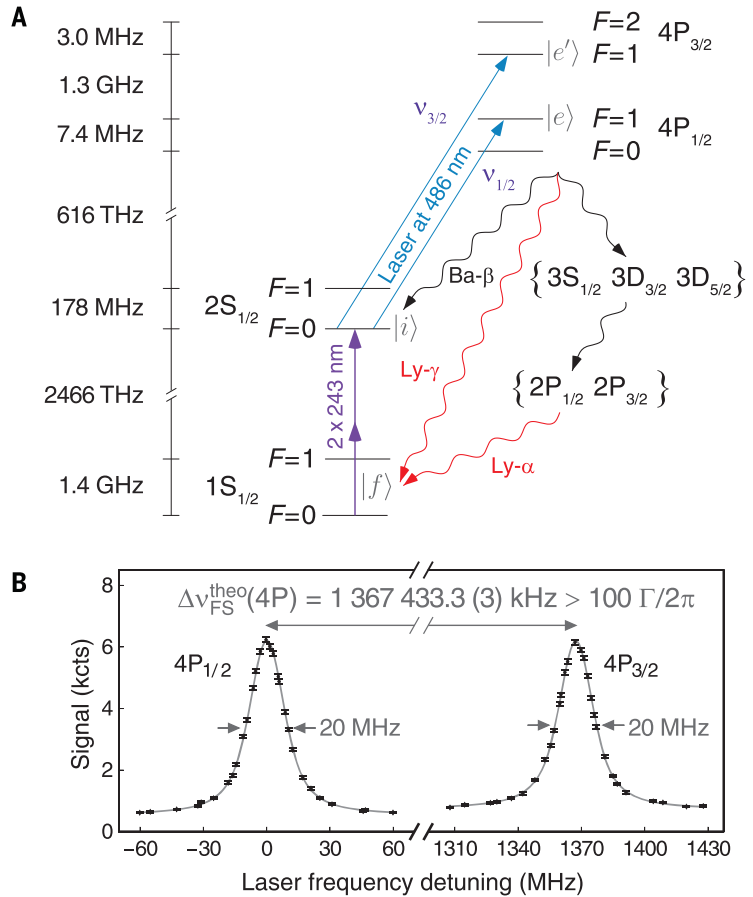
(A) Relevant energy levels for hydrogen 2S-4P spectroscopy are shown (not to scale). The atoms are prepared in the  $2S_{1/2}^{F=0}$  metastable state ( $|i\rangle$ ) by two-photon excitation with a preparation laser at 243 nm. The spectroscopy laser at 486 nm drives the one-photon  $2S_{1/2}^{F=0}$  to  $4P_{1/2}^{F=1}$  ( $|e\rangle$ ) and  $4P_{3/2}^{F=1}$  ( $|e'\rangle$ ) states to determine the transition frequencies  $\nu_{1/2}$  and  $\nu_{3/2}$ , respectively.

These states

decay rapidly, predominantly to the 1S ground state ( $|f\rangle$ ) either directly through Lyman- $\gamma$  fluorescence at 97 nm (Ly- $\gamma$ , branching ratio 84%) or indirectly through the 3S, 3D, and 2P levels, yielding one Lyman- $\alpha$  photon at 121 nm (Ly- $\alpha$ , branching ratio 4%). The remaining 12% of the decays lead back to the 2S state through Balmer- $\beta$  decay (Ba- $\beta$ ), with 4% decaying back to the initial  $2S_{1/2}^{F=0}$  state. Excitations from the  $2S_{1/2}^{F=0}$  to the  $4P_{1/2}^{F=0}$  and  $4P_{3/2}^{F=2}$  levels are forbidden by angular momentum conservation. (B) Typical experimental fluorescence signal from a single line scan over the 2S-4P<sub>1/2</sub> (left) and 2S-4P<sub>3/2</sub> (right) resonance (black diamonds). The observed line width (full width at half maximum) of  $\sim 2\pi \times 20$  MHz is larger than the natural line width  $\Gamma = 2\pi \times 12.9$  MHz because of Doppler and power broadening. The accuracy of our measurement corresponds to almost 1 part in 10,000 of the observed line width. The constant background counts are caused by the decay of 2S atoms inside the detector (17). kcts, kilocounts.

shift is reduced to 45 kHz, corresponding to five times the proton radius discrepancy.

One way to model this shift is to perform elaborate simulations of the entire experiment by numerical integration of the optical Bloch equations (OBE), including all relevant intermediate states and, importantly, the often-neglected cross-damping terms between them leading to quantum interference (18, 20, 22–26). The results of this simulation then have to be evaluated for the experimental geometry, a requirement that may be difficult to meet with sufficient accuracy. For the  $2S \rightarrow \{4P_{1/2}, 4P_{3/2}\} \rightarrow 1S$  excitation spectrum considered here, this simulation consists of a total number of 2707 coupled, complex-valued ordinary differential equations. We have performed such an OBE simulation of the experiment using high-performance computation resources provided by the Max Planck Computing and



Data Facility. By taking into account our experimental geometry with a sophisticated model, including particle tracing of the detected photoelectrons, the simulation is able to explain the measured data very well (see dashed line in Fig. 4, A and B). However, it is challenging to reliably estimate the uncertainty of the modeling of the detection geometry that dominates the simulation uncertainty.

Realizing that the natural line shape of the  $2S \rightarrow \{4P_{1/2}, 4P_{3/2}\} \rightarrow 1S$  excitation spectrum can also be parametrized according to Eq. 3, a much simpler data analysis is possible. This only requires one additional free parameter,  $b/C$ , which encodes the experimental geometry (we have dropped the negligible term proportional to  $a$ ). For sufficiently low excitation rates such as in this experiment, the influence of quantum interference will then lead to a nonzero  $b/C$ , but the



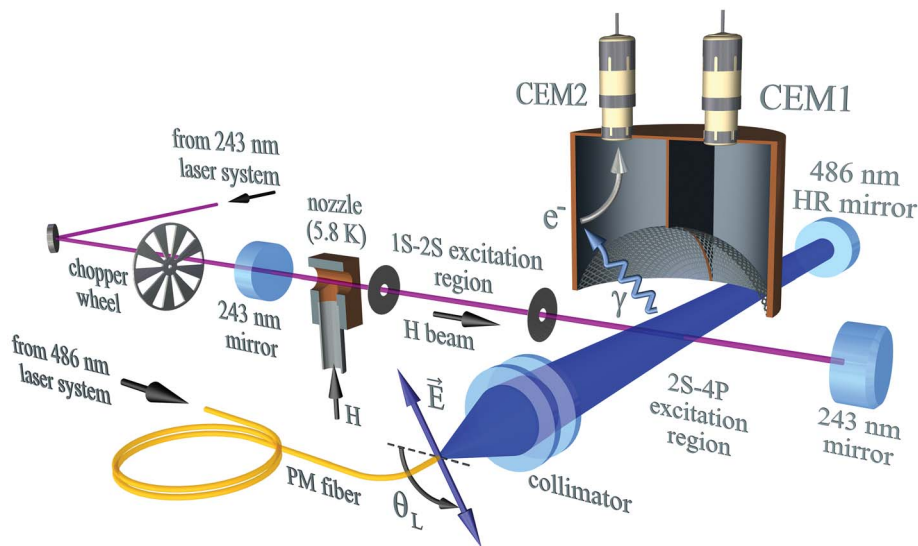


**Fig. 3. Experimental apparatus (not to scale).** A preparation laser at 243 nm is used to excite hydrogen atoms that emerge from the cold copper nozzle (5.8 K) from the ground state to the 2S state. The 2S-4P transition is driven with the spectroscopy laser at 486 nm. This laser is coupled to an active fiber-based retroreflector [consisting of polarization-maintaining (PM) fiber, collimator, and high-reflectivity (HR) mirror] oriented perpendicular to the atomic beam; this setup provides a large suppression of the first-order Doppler effect (36). In the dark phases of the chopper wheel, Lyman- $\gamma$  fluorescence photons ( $\gamma$ ) emitted upon the rapid 4P $\rightarrow$ 1S decay are detected via photoelectrons ( $e^-$ ) by channel electron multipliers CEM1 and CEM2. The two detectors are separated by a vertical wall along the direction of the 486-nm light propagation. The 2S-4P excitation region is shielded from stray electric fields (with dedicated meshes) and magnetic fields (with magnetic shielding, not shown), resulting in stray fields below 0.6 V/m and 1 mG, respectively (17). The blue double-sided arrow labeled  $\vec{E}$  indicates the electric field of the 486-nm spectroscopy laser with orientation  $\theta_L$  against the horizontal.

extracted line center  $\omega_0$  will not be shifted with respect to its unperturbed value. In contrast to the OBE simulation, the influence of the experimental geometry can be precisely extracted from the spectroscopy data, rather than required as an external input.

To also take into account Gaussian broadening mechanisms, such as the atomic beam divergence in our experiment detailed below, the expanded line shape (Eq. 3) is convolved with a Gaussian of width  $\Gamma_G$  (full width at half maximum). Again omitting the small linear term proportional to  $a$ , this yields what we in the following will refer to as Fano-Voigt line shape (17, 31, 32)

$$\mathcal{F}(\omega) = A \{ \text{Re}[w(z)] + 2\eta \text{Im}[w(z)] \} \quad (5)$$

where  $w(z)$  denotes the Faddeeva function of the argument  $z = 2\sqrt{\ln 2}[(\omega - \omega_0) + i\Gamma/2]/\Gamma_G$ . Analogous to Eq. 3, the Fano-Voigt line shape consists of a Voigt profile, corresponding to the convolution of the Gaussian and the Lorentzian profile, and a dispersive-shaped perturbation. The asymmetry parameter  $\eta = b\Gamma/4C$  measures the amplitude of this perturbation relative to the observed line strength  $A$  and directly gives the line shift, in units of the observed line width, that is canceled by including the perturbation.

Additional line shifts caused by the interplay of quantum interference with both the back decay of the 4P state to the initial 2S state and the

depletion of this initial state are not fully accounted for by the Fano-Voigt line shape but could in principle be removed by using an even more sophisticated line shape. However, those additional shifts are considerably smaller and less geometry-dependent than the shift removed by the Fano-Voigt line shape. Thus, we apply small model corrections to the data [1.3(2) kHz for the most affected 2S-4P $_{1/2}$  transition] determined by fitting the Fano-Voigt line shape to the OBE simulations (17). Note that these additional shifts also have opposite signs for the two mutually perturbing resonances. Although the bulk of the broadening caused by the atomic beam divergence and saturation effects is well described by the Fano-Voigt line shape, small deviations symmetric about the line center remain. In combination with an imperfectly symmetric experimental sampling of the resonance about its center, this can lead to a sampling bias in the determined line centers. We reduce this sampling bias by selectively removing a small amount of experimental points to enforce fair sampling (17). The remaining sampling bias is estimated with a Monte Carlo simulation using the experimental sampling and signal-to-noise ratio, leading to a maximum correction of 0.8(0.7) kHz.

### Experimental setup

To measure the 2S-4P transition frequency and study the effect of quantum interference, we use

the dedicated setup depicted in Fig. 3 (33–35). A cryogenic beam of H in the metastable 2S state obtained from Doppler-free two-photon excitation of the 1S-2S transition is crossed at right angles with radiation from the spectroscopy laser at 486 nm, driving the 2S-4P transition. The hyperfine splitting in the 2S state is resolved in the 1S-2S excitation, so that the atoms are almost exclusively prepared in the 2S $_{1/2}^{F=0}$  sublevel. From this state, only two dipole-allowed transitions may be driven as depicted in Fig. 2, either to the 4P $_{1/2}^{F=1}$  state (2S-4P $_{1/2}$  transition) or to the 4P $_{3/2}^{F=1}$  state (2S-4P $_{3/2}$  transition). The linear polarization of the spectroscopy laser is oriented at angle  $\theta_L$  to the horizontal and defined by a polarization-maintaining (PM) fiber (intensity polarization extinction ratio 200:1). The polarization can be rotated about the laser beam axis by either making use of the two orthogonal PM axes of the fiber or rotating the fiber itself.

To observe the effects of quantum interference more clearly, we have split our large solid angle detector by a vertical wall along the spectroscopy laser beam, creating two detectors that observe the fluorescence of the 4P state from different directions, but with the same solid angle. The Lyman- $\gamma$  extreme ultraviolet photons emitted upon this rapid decay of the short-lived 4P state to the 1S ground state release photoelectrons from the graphite-coated inner walls of the detectors, which are counted by two channel electron multipliers, CEM1 and CEM2; the output of these multipliers is our signal.

### Doppler shift

The mean thermal velocity of atoms in our cryogenic beam is about 300 m/s, 10 times smaller than in previous experiments. In addition, a high level of compensation of the first-order Doppler shift is achieved by using an active fiber-based retroreflector specifically developed for this experiment (36). The transition is driven by two phase-retracing antiparallel laser beams, leading to Doppler shifts of opposite sign and equal amplitude for atoms being excited by the respective beams. To verify this scheme, we probe atomic samples with mean velocities ranging from 295 down to 85 m/s. These low velocities are achieved by quickly switching off the 1S-2S excitation light at 243 nm and letting the fastest 2S atoms escape before acquiring data (time-of-flight resolved detection scheme). Any residual first-order Doppler shift can be constrained by extracting the rate of change of the observed transition frequency with the mean velocity of the atoms interrogated for each delay time. We extract this Doppler slope from the same data used to determine the transition frequencies presented here and find it to be compatible with zero for each transition after averaging all our data. The corresponding frequency uncertainty is found by multiplying the Doppler slope with the mean velocity of all atoms interrogated, 240 m/s, giving an uncertainty of 2.9 and 2.8 kHz for the 2S-4P $_{1/2}$  and the 2S-4P $_{3/2}$  transitions, respectively. The two antiparallel laser beams weakly couple different momentum eigenstates of the 2S atoms and can drive Raman

transitions between them. Because the coupling is detuning dependent, it can lead to small line shifts, which we evaluate with an auxiliary OBE simulation that takes into account the recoil of the atoms. For our atomic beam geometry and excitation rates, this light force shift is found to be below 0.5 kHz for both transitions measured (17).

Although the laser beam configuration resembles the well-known saturated absorption configuration, the characteristic dip in the line shape expected for this configuration is not present here because the Doppler width of the atomic beam closely matches the natural line width of the 2S-4P transition and we work in the low-saturation regime.

### Observation of quantum interference line shifts

Figure 4 shows the effects of quantum interference line distortions for the 2S-4P<sub>1/2</sub> and 2S-4P<sub>3/2</sub> transitions. Data were acquired at different orientations  $\theta_L$  of the linear laser polarization (see Fig. 3) and thus for different orientations of the induced atomic dipole relative to the field of view of the detectors. The data set consists of a total number of 22,928 and 25,064 individual resonances for the 2S-4P<sub>1/2</sub> and 2S-4P<sub>3/2</sub> transitions, respectively, with varying amounts of resonances recorded per  $\theta_L$  setting.

By using the Voigt approximation ( $\eta = 0$  in Eq. 5) as line shape model, a  $\theta_L$  dependence of the extracted resonance frequency is observed for both transitions and detectors (Fig. 4, A and B). The amplitudes of the shift of 40 and 20 kHz for the 2S-4P<sub>1/2</sub> and 2S-4P<sub>3/2</sub> transitions, respectively, are much larger than the proton radius discrepancy of 8.9 kHz. Although averaging over  $\theta_L$  reduces the shift, it does not average to zero and a significant shift of 6.8 and -3.0 kHz remains for the two transitions, respectively, as determined from our simulation. As expected from Eq. 4, the shifts of the two mutually perturbing transitions are of opposite signs; as expected from the symmetry of the experimental geometry, exchanging the two detectors corresponds to mirroring the laser polarization about the vertical ( $\theta_L = 90^\circ$ ). The behavior is well reproduced by our simulation (dashed lines in Fig. 4), confirming that the detection geometry has been correctly taken into account. This is a direct observation of a quantum interference line shift in the regime of large separation between the atomic resonances ( $\Delta/\Gamma > 100$ ); for the unresolved D2 lines in lithium ( $\Delta/\Gamma \approx 1$ ), similar effects have been observed before (29, 37).

Fitting the resonances with the Fano-Voigt line shape, on the other hand, removes the  $\theta_L$  dependence (Fig. 4, C and D), with the geometry dependence now absorbed in the asym-

metry parameter  $\eta$ . The residual amplitudes ( $A_{\text{res}}$ , dotted lines in Fig. 4) of possible remaining quantum interference shifts are determined by fitting a parametrized version of our simulation to the data and are found to be well compatible with zero, except for a 3.2(1.2) kHz effect for the CEM1 data of the 2S-4P<sub>1/2</sub> transition. When averaging over  $\theta_L$  and both detectors to determine the 2S-4P<sub>1/2</sub> and 2S-4P<sub>3/2</sub> transition frequencies, this results in insignificant residual shifts of 0.3(3) and 0.0(3) kHz, respectively (17). Because the Doppler shift uncertainty on the order of 10 kHz per point is correlated between the two line shape models, it is not included in the error bars shown in Fig. 4 to highlight the difference between the models. When including the Doppler shift and systematic uncertainties (red-shaded area in Fig. 4), we see only a small scatter of the data points, with the notable exception of the points for  $0^\circ$  and  $90^\circ$  for the 2S-4P<sub>1/2</sub> transition. These points were taken during the first two days of the measurement where the larger observed line width suggests a slight misalignment between the 2S-4P excitation laser and the atomic beam. However, discarding these data would only shift the final result (Eq. 9) by an insignificant 0.3 kHz.

### 2S-4P absolute transition frequency

Having removed the influence of quantum interference by using the Fano-Voigt line shape, we

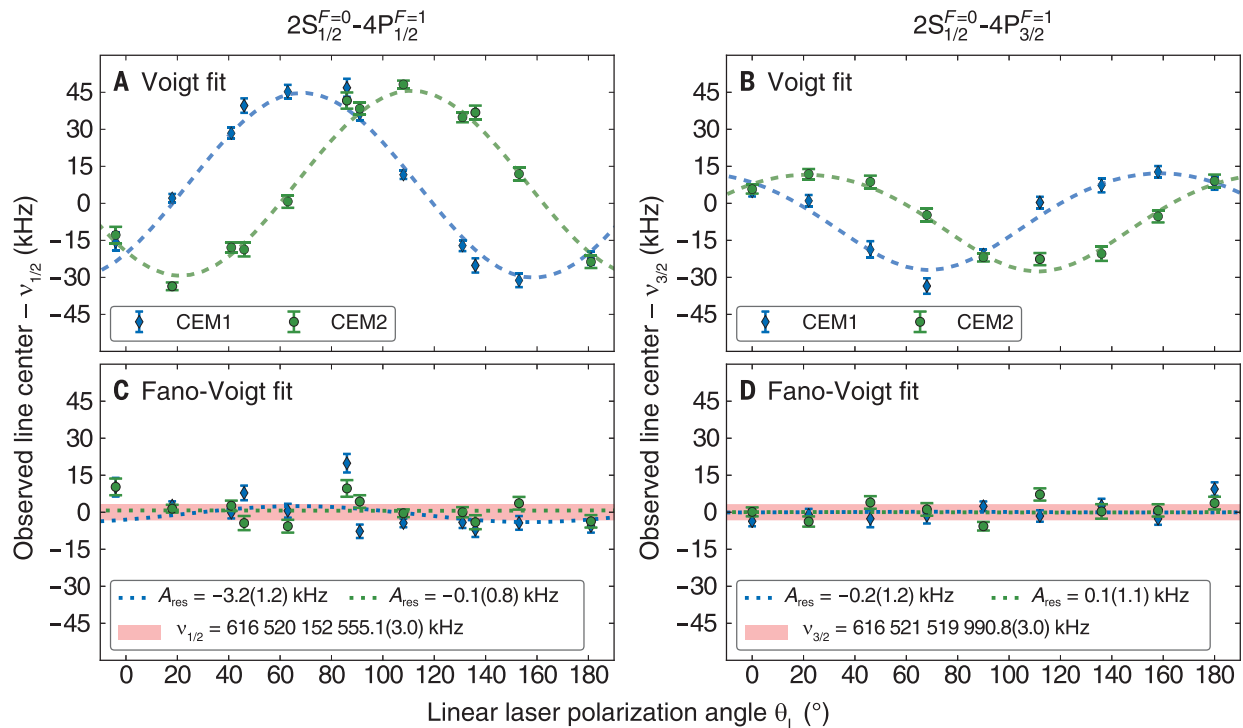


**Fig. 4. Observation of quantum interference.** Shown are apparent line shifts caused by quantum interference (A and B) and their suppression (C and D). Observed line centers of the 2S-4P<sub>1/2</sub> (A) and 2S-4P<sub>3/2</sub> (B) transitions determined with symmetric Voigt fits show a dependence on the direction of the linear laser polarization  $\theta_L$  with an amplitude of up to 40 kHz in our geometry. Our numerical simulation (dashed lines) reproduces this behavior very well (17). Using the Fano-Voigt

line shape (Eq. 5) removes the  $\theta_L$  dependence (C) and (D). Blue and green symbols indicate data recorded with CEM1 and CEM2, respectively (see Fig. 3). Error bars indicate the statistical uncertainty only. The red-shaded areas (17) show the weighted mean of both detectors, including the final uncertainty dominated by the Doppler shift uncertainty. The dotted lines show an estimate of possible remaining line shifts with amplitude  $A_{\text{res}}$ .

Table 1. List of corrections  $\Delta\nu$  and uncertainties  $\sigma$  for the determination of the 2S-4P fine structure centroid  $\nu_{2S-4P}$ . See (17) for details.

Contribution	$\Delta\nu$ (kHz)	$\sigma$ (kHz)
Statistics	0.00	0.41
First-order Doppler shift	0.00	2.13
Quantum interference shift	0.00	0.21
Light force shift	-0.32	0.30
Model corrections	0.11	0.06
Sampling bias	0.44	0.49
Second-order Doppler shift	0.22	0.05
dc-Stark shift	0.00	0.20
Zeeman shift	0.00	0.22
Pressure shift	0.00	0.02
Laser spectrum	0.00	0.10
Frequency standard (hydrogen maser)	0.00	0.06
Recoil shift	-837.23	0.00
Hyperfine structure corrections	-132,552.092	0.075
Total	-133,388.9	2.3

can now give the unperturbed transition frequencies by averaging over the different laser polarization settings and both detectors. The laser frequency has been determined with a frequency comb linked to a Global Positioning System (GPS)-referenced hydrogen maser. For the transition frequencies from the  $2S_{1/2}^{F=0}$  state to the  $4P_{1/2}^{F=1}$  state ( $\nu_{1/2}$ ) and the  $4P_{3/2}^{F=1}$  state ( $\nu_{3/2}$ ), we find

$$\nu_{1/2} = 616520152555.1(3.0) \text{ kHz} \tag{6}$$

$$\nu_{3/2} = 616521519990.8(3.0) \text{ kHz} \tag{7}$$

where the given uncertainties include both statistical and systematic uncertainties and are dominated by the Doppler shift uncertainty. This result corresponds to an improvement of a factor of 4.9 and 3.3 in uncertainty, respectively, compared to the previous best measurements of the 2S-4P<sub>1/2</sub> and 2S-4P<sub>3/2</sub> transitions (16). The values in Eqs. 6 and 7 have been corrected for the recoil shift of 837.23 kHz. Details of the data analysis and a list of corrections and uncertainties are given in (17) (see table S2).

We subtract  $\nu_{1/2}$  from  $\nu_{3/2}$  to obtain the 4P fine structure splitting  $\Delta\nu_{FS}^{exp}(4P)$  between the  $4P_{1/2}^{F=1}$  and the  $4P_{3/2}^{F=1}$  states (17) (see table S3)

$$\Delta\nu_{FS}^{exp}(4P) = 1367435.7(4.3) \text{ kHz} \tag{8}$$

The fine structure splitting is essentially free from finite-size corrections and can therefore be calculated very precisely (38), yielding  $\Delta\nu_{FS}^{theo}(4P) = 1367433.3(3) \text{ kHz}$ . With a difference of 2.4 (4.3) kHz, our experimental result is in excellent agreement with the theoretical value. Furthermore, it represents the most accurately determined fine structure splitting in H inferred from an optical transition frequency measurement.

Even more importantly, because any shifts caused by quantum interference will be of opposite signs for the two resonances, the comparison of  $\Delta\nu_{FS}^{exp}(4P)$  and  $\Delta\nu_{FS}^{theo}(4P)$  provides a sensitive measure for residual quantum interference shifts and an independent test of the internal consistency of our data analysis. If not accounted for, the quantum interference line shifts would lead to a discrepancy of about 10 kHz between  $\Delta\nu_{FS}^{exp}(4P)$  and  $\Delta\nu_{FS}^{theo}(4P)$  in our measurement, when the signal is averaged over all polarization angles and both detectors. To increase the sensitivity of this test further, one can compare data for laser polarizations where the line shifts are largest, e.g., at  $\theta_L \approx 110^\circ$  for CEM2. Here, the difference of the splitting to the theory value is 10.0(16.9) kHz, after the Fano-Voigt line shape has compensated for an ~70-kHz shift.

To make use of the fact that the quantum interference effects, including those not compensated for by the Fano-Voigt line shape and accounted for by small model corrections, shift the two resonances in opposite directions, it is advantageous to determine the transition frequency from the 2S hyperfine centroid to the 4P fine structure centroid [i.e., the centroid of the hyperfine centroids; see eq. S16 in (17)] using Eqs. 6 and 7

$$\nu_{2S-4P} = 616520931626.8(2.3) \text{ kHz} \tag{9}$$

With this combination, the model correction and the upper limit on possible residual line shifts caused by quantum interference are reduced to a negligible 0.1(1) and 0.2 kHz, respectively. The final measurement uncertainty of 2.3 kHz is four times smaller than the proton radius discrepancy for the 2S-4P transition. The uncertainty is dominated by the first-order Doppler shift uncertainty, given by the weighted average

of the corresponding uncorrelated uncertainties for the 2S-4P<sub>1/2</sub> and 2S-4P<sub>3/2</sub> transitions. A list of the corrections applied and the contributions to the total uncertainty is given in Table 1.

Rydberg constant and proton charge radius

Following (3), we combine Eq. 9 with our previous measurement of the 1S-2S transition frequency (1, 2) to determine the value pair [ $R_\infty$ ,  $r_p$ ] using Eq. 1

$$R_\infty = 10973731.568076(96) \text{ m}^{-1} \tag{10}$$

$$r_p = 0.8335(95) \text{ fm} \tag{11}$$

providing the most accurate determination of these values from H spectroscopy with uncertainties equivalent to the aggregate H world data. We find good agreement with the  $\mu p$  value (4, 5), but a discrepancy of 3.3 combined standard deviations to the H world data (see Fig. 1) for both  $R_\infty$  and  $r_p$ . Our new value for  $R_\infty$  also agrees with the one obtained from the combination of the muonic deuterium measurement (13) and the 1S-2S transition frequency in electronic deuterium (39).

Previous H experiments almost exclusively used the depletion of the 2S initial state population to detect 2S- $nL$  excitations in a number of different detection geometries. These schemes are generally much less prone to the effects of quantum interference. This advantage, however, comes at the price of a considerably reduced signal-to-noise ratio (compared to our fluorescence-detection scheme), which makes the identification and study of small systematic shifts much more difficult. Averaging results from various sources (i.e., geometries) may further be expected to cancel the potential residual shifts caused by quantum interference to some extent so that it seems rather unlikely that this effect can explain the observed discrepancy with the H world data.

The discrepancy of the results in this work with the H world data limits the precision of tests of bound-state QED. Provided that QED calculations are correct, new experiments with improved accuracy will help to understand the discrepancy. Several of such experiments using various approaches are currently under way (40–48). The tools developed in this work for 2S-4P spectroscopy can now be applied to other 2S- $nP$  transitions to provide additional experimental data.

REFERENCES AND NOTES

1. C. G. Parthey et al., *Phys. Rev. Lett.* **107**, 203001 (2011).  
2. A. Matveev et al., *Phys. Rev. Lett.* **110**, 230801 (2013).  
3. P. J. Mohr, D. B. Newell, B. N. Taylor, *Rev. Mod. Phys.* **88**, 035009 (2016).  
4. R. Pohl et al., *Nature* **466**, 213–216 (2010).  
5. A. Antognini et al., *Science* **339**, 417–420 (2013).  
6. R. Pohl, R. Gilman, G. A. Miller, K. Pachucki, *Annu. Rev. Nucl. Part. Sci.* **63**, 175–204 (2013).  
7. J. C. Bernauer, R. Pohl, *Sci. Am.* **310**, 32–39 (2014).  
8. C. E. Carlson, *Prog. Part. Nucl. Phys.* **82**, 59–77 (2015).  
9. J. C. Bernauer et al., *Phys. Rev. Lett.* **105**, 242001 (2010).  
10. X. Zhan et al., *Phys. Lett. B* **705**, 59–64 (2011).

11. J. Arrington, I. Sick, *J. Phys. Chem. Ref. Data* **44**, 031204 (2015).
12. H world data corresponds to adjustment 8, table XXIX in (3).
13. R. Pohl *et al.*, *Science* **353**, 669–673 (2016).
14. B. de Beauvoir *et al.*, *Eur. Phys. J. D* **12**, 61–93 (2000).
15. B. de Beauvoir *et al.*, *Eur. Phys. J. D* **14**, 398 (2001).
16. D. J. Berkeland, E. A. Hinds, M. G. Boshier, *Phys. Rev. Lett.* **75**, 2470–2473 (1995).
17. Materials and methods are available as supplementary materials.
18. M. Horbatsch, E. A. Hessels, *Phys. Rev. A* **82**, 052519 (2010).
19. D. J. Berkeland, thesis, Yale University (1995).
20. A. Marsman, M. Horbatsch, E. A. Hessels, *J. Phys. Chem. Ref. Data* **44**, 031207 (2015).
21. G.-P. Feng, X. Zheng, Y. R. Sun, S.-M. Hu, *Phys. Rev. A* **91**, 030502 (2015).
22. M. Horbatsch, E. A. Hessels, *Phys. Rev. A* **84**, 032508 (2011).
23. A. Marsman, M. Horbatsch, E. A. Hessels, *Phys. Rev. A* **86**, 012510 (2012).
24. A. Marsman, M. Horbatsch, E. A. Hessels, *Phys. Rev. A* **86**, 040501 (2012).
25. A. Marsman, E. A. Hessels, M. Horbatsch, *Phys. Rev. A* **89**, 043403 (2014).
26. D. C. Yost *et al.*, *Phys. Rev. A* **90**, 012512 (2014).
27. R. Loudon, *The Quantum Theory of Light* (Oxford Univ. Press, 1983).
28. U. D. Jentschura, P. J. Mohr, *Can. J. Phys.* **80**, 633–644 (2002).
29. R. C. Brown *et al.*, *Phys. Rev. A* **87**, 032504 (2013).
30. U. Fano, *Phys. Rev.* **124**, 1866–1878 (1961).
31. S. Schippers, *Int. Rev. At. Mol. Phys.* **2**, 151–156 (2011).
32. S. Schippers, Analytical expression for the convolution of a Fano line profile with a Gaussian. arXiv:1203.4281v2 [physics.atom-ph] (13 May 2016).
33. A. Beyer *et al.*, *J. Phys. Conf. Ser.* **467**, 012003 (2013).
34. A. Beyer *et al.*, *Phys. Scr.* **T165**, 014030 (2015).
35. A. Beyer *et al.*, *Ann. Phys.* **525**, 671–679 (2013).
36. A. Beyer *et al.*, *Opt. Express* **24**, 17470–17485 (2016).
37. C. J. Sansonetti *et al.*, *Phys. Rev. Lett.* **107**, 023001 (2011).
38. M. Horbatsch, E. A. Hessels, *Phys. Rev. A* **93**, 022513 (2016).
39. R. Pohl *et al.*, *Metrologia* **54**, L1–L10 (2017).
40. A. C. Vutha *et al.*, *Bull. Am. Phys. Soc.* **57**, D1138 (2012).
41. S. Galtier *et al.*, *J. Phys. Chem. Ref. Data* **44**, 031201 (2015).
42. D. C. Yost *et al.*, *Phys. Rev. A* **93**, 042509 (2016).
43. M. Puchalski, J. Komasa, P. Czachorowski, K. Pachucki, *Phys. Rev. Lett.* **117**, 263002 (2016).
44. J. Liu *et al.*, *J. Chem. Phys.* **130**, 174306 (2009).
45. D. Sprecher, J. Liu, C. Jungen, W. Ubachs, F. Merkt, *J. Chem. Phys.* **133**, 111102 (2010).
46. J.-P. Karr, L. Hilico, J. C. J. Koelemeij, V. I. Korobov, *Phys. Rev. A* **94**, 050501 (2016).
47. R. K. Altmann, S. Galtier, L. S. Dreissen, K. S. E. Eikema, *Phys. Rev. Lett.* **117**, 173201 (2016).
48. U. D. Jentschura, P. J. Mohr, J. N. Tan, *J. Phys. B* **43**, 074002 (2010).

#### ACKNOWLEDGMENTS

The authors thank E. A. Hessels and U. D. Jentschura for insightful discussions and W. Simon, K. Linner, and H. Brückner for technical support. K.K. and N.K. acknowledge support from Russian Science Foundation 16-12-00096, R.P. from the European Research Council (ERC) Starting Grant #279765, and T.W.H. from the Max Planck Foundation. The data underlying this study are available from the corresponding author upon reasonable request.

#### SUPPLEMENTARY MATERIALS

[www.sciencemag.org/content/358/6359/79/suppl/DC1](http://www.sciencemag.org/content/358/6359/79/suppl/DC1)  
Materials and Methods

Fig. S1

Tables S1 to S3

References (49–59)

28 July 2016; accepted 28 August 2017

10.1126/science.aah6677

## The Rydberg constant and proton size from atomic hydrogen

Axel Beyer, Lothar Maisenbacher, Arthur Matveev, Randolph Pohl, Ksenia Khabarova, Alexey Grinin, Tobias Lamour, Dylan C. Yost, Theodor W. Hänsch, Nikolai Kolachevsky and Thomas Udem

*Science* **358** (6359), 79-85.  
DOI: 10.1126/science.aah6677

### How big is the proton?

The discrepancy between the size of the proton extracted from the spectroscopy of muonic hydrogen and the value obtained by averaging previous results for "regular" hydrogen has puzzled physicists for the past 7 years. Now, Beyer *et al.* shed light on this puzzle (see the Perspective by Vassen). The authors obtained the size of the proton using very accurate spectroscopic measurements of regular hydrogen. Unexpectedly, this value was inconsistent with the average value of previous measurements of the same type. Also unexpectedly, it was consistent with the size extracted from the muonic hydrogen experiments. Resolving the puzzle must now include trying to understand how the old results relate to the new, as well as reexamining the sources of systematic errors in all experiments.

*Science*, this issue p. 79; see also p. 39

#### ARTICLE TOOLS

<http://science.sciencemag.org/content/358/6359/79>

#### SUPPLEMENTARY MATERIALS

<http://science.sciencemag.org/content/suppl/2017/10/04/358.6359.79.DC1>

#### RELATED CONTENT

<http://science.sciencemag.org/content/sci/358/6359/39.full>

#### REFERENCES

This article cites 50 articles, 2 of which you can access for free  
<http://science.sciencemag.org/content/358/6359/79#BIBL>

#### PERMISSIONS

<http://www.sciencemag.org/help/reprints-and-permissions>

Use of this article is subject to the [Terms of Service](#)

---

*Science* (print ISSN 0036-8075; online ISSN 1095-9203) is published by the American Association for the Advancement of Science, 1200 New York Avenue NW, Washington, DC 20005. The title *Science* is a registered trademark of AAAS.

Copyright © 2017 The Authors, some rights reserved; exclusive licensee American Association for the Advancement of Science. No claim to original U.S. Government Works